# Valence can control the non-exponential viscoelastic relaxation of reversible multivalent gels

Hugo Le Roy,[1,*] Jake Song,[2] Gareth H. McKinley,[3] Niels Holten-Andersen,[2] and Martin Lenz[1,4,†]

[1] *Université Paris-Saclay, CNRS, LPTMS, 91405, Orsay, France*
[2] *Department of Materials Science and Engineering, Massachusetts Institute of Technology, 77 Massachusetts Avenue, Cambridge, MA 02139, USA*
[3] *Department of Mechanical Engineering, Massachusetts Institute of Technology, 77 Massachusetts Avenue, Cambridge, MA 02139, USA*
[4] *PMMH, CNRS, ESPCI Paris, PSL University, Sorbonne Université, Université de Paris, F-75005, Paris, France*

Hydrogels connected by multivalent reversible crosslinkers are a versatile design platform for biocompatible viscoelastic materials. Their linear response to a step strain displays a fast, exponential relaxation when using low valence crosslinkers, while larger supramolecular crosslinkers bring about much slower dynamics involving a wide distribution of time scales whose physical origin is still debated. Here, we are proposing a model where the gels' relaxation originate from elementary events in which the bonds connecting two neighboring crosslinkers all disconnect. Larger crosslinkers allow for a greater average number of bonds connecting them, but also generate more heterogeneity. We characterize the resulting distribution of relaxation time scales analytically, and accurately reproduce rheological measurement on metal-coordinate hydrogels with a variety of crosslinker sizes including ions, metal-organic cages, and nanoparticles. Our approach is simple enough to be extended to any crosslinker size, and could thus be harnessed for the rational design of complex viscoelastic materials.

Soft hydrogels are ubiquitous in biology, and dictate the mechanics of cells and tissues [1]. Due to their biocompatibility, synthetic hydrogels are prime candidates to serve as robust soft tissue implants, although a fine control of their viscoelastic properties is crucial for their success in this role [2, 3]. In addition to standard approaches based on polymer rigidity and concentration [4, 5], a new design strategy based on nanocomposite hydrogels has recently emerged [6]. In these materials, large crosslinkers such as clay [7], latex beads [8], or metal-coordinate nanoparticles [9] are embedded in a standard polymer matrix to make it stronger [10, 11]. Using transient crosslinkers combines these benefits with a viscoelastic relaxation over long time scales [12] as the crosslinkers unbind, relax and rebind to the polymers.

The viscoelastic response of nanocomposite hydrogels depends on the size of their crosslinkers. Metal-coordinate gels crosslinked by single ions thus display a single-exponential, Maxwell-like linear viscoelastic response to a step strain [13]. Multiple types of ions can then be combined in a single material to achieve complex relaxational dynamics over up to a few tens of seconds [14]. To achieve longer relaxation times, larger crosslinkers allowing dozens of polymers to bind are typically needed, and bring about a more solid-like behavior [15]. This in turns brings about a more complex relaxational dynamics. The resulting stress response to a step strain is often fairly well described by a stretched exponential:

$$\sigma(t) \propto \exp\left[-(t/\tau)^{\alpha}\right], \tag{1}$$

where smaller values of the stretching exponent $\alpha \in ]0;1[$ denote broader distributions of relaxation time scales [16]. This phenomenological law does not however have an obvious physical interpretation, and the origin of the nontrivial dependence of $\alpha$ and $\tau$ on temperature and the crosslinker size remains unclear. A similarly phenomenological power law ($\sigma \propto t^{-\beta}$) fit is often applied to the rheology of other soft materials [17–19].

Here we aim to elucidate the response and enable the

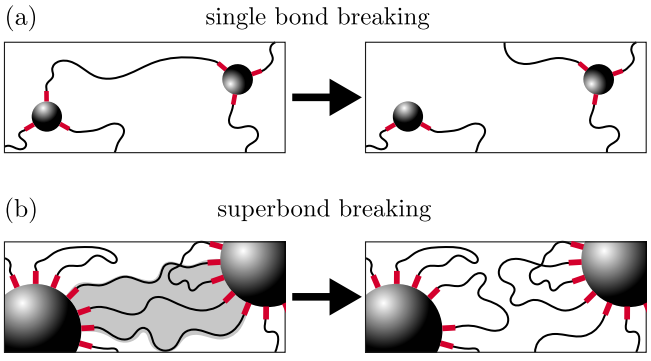


FIG. 1. High-valence crosslinkers yield a slow, potentially complex unbinding dynamics (a) Hydrogels held together by small crosslinkers relax over the time scale associated with the unbinding of a single polymer strand. (b) By contrast, relaxation events in the presence of high-valence crosslinkers require the simultaneous unbinding of many polymer stands. The associated time scale is long and highly variable depending on the number of strands involved in the "superbond" (grey shade).

* hugo.le-roy@universite-paris-saclay.fr
† martin.lenz@universite-paris-saclay.fr

rational design of soft materials with crosslinkers that display a high valence. We use the term "valence" to designate the number of polymer strands that a crosslinker can bind, a property sometimes also refered to as their "functionality". We develop a physical model of their viscoelastic relaxation. While existing microscopic rationalizations of stretched exponential relaxation are often based on collective rearrangements in glass-like, dense assemblies of hard particles [20], nonlinear elastic response regimes [21] or the distribution of the sizes of the material's constitutive units [22], none of these is straightforwardly applicable here. Instead, we propose that the elementary relaxation events in viscoelastic gels with high-valence crosslinkers resemble those at play in the presence of low-valence ions, where stress is released by the severing of the physical connection between two crosslinkers (Fig. 1). In the case of high-valence crosslinkers, such connections–hereafter termed "superbonds"–are comprised of several polymer strands. We find that the breaking time of a superbond strongly depends on the number of strands involved, consistent with previous observations [23]. As a result of this dependence, small spatial heterogeneities in the polymer concentration may result in widely different relaxation times from one superbond to the next. This exponential amplification of small structural differences is reminiscent of models previously used to describe the relaxation of soft glasses [24, 25]. In contrast with these previous studies, our approach explicitly models their microscopic basis and allows us to successfully account for the influence of temperature and crosslinker valence on the macroscopic stress relaxation observed in the resulting gel.

We model the attachment and detachment of a single polymer strand from a pair of crosslinkers as shown in Fig. 2(a). The energy barrier $\Delta E$ to disconnect the polymer from a crosslinker and go into the transition state is much larger than the thermal energy $k_BT = \beta^{-1}$, implying that the transition state is short-lived. Assuming a completely flexible polymer strand, the attached and detached state on either side of this transition have the same energy (equal to $-\Delta E$), but their entropy may differ by an amount $\Delta S$. The overall rate $\omega^+$ to go from the detached to the attached state ($\omega^-$ for the reverse) thus reads

$$\omega^+ = \frac{1}{\tau_0} e^{-\beta\Delta E} \qquad \omega^- = \frac{1}{\tau_0} e^{-\beta\Delta E + \Delta S}, \tag{2}$$

where any difference in entropy between the detached and transition state is hidden in the characteristic time scale $\tau_0$ [26]. At equilibrium, we denote the probability for a single polymer strand to be attached as $p_{\text{on}} = 1 - p_{\text{off}} = 1/(1 + e^{\Delta S})$.

We now consider the dynamics of a superbond involving $N$ polymer strands and assume that each strand attaches and detaches independently from the others. As a result the superbond undergoes the Markov process illustrated in Fig. 2(b), and the probability $P(n, t)$ for $n$ strands to connect the two crosslinkers at time $t$ satisfies the master equation

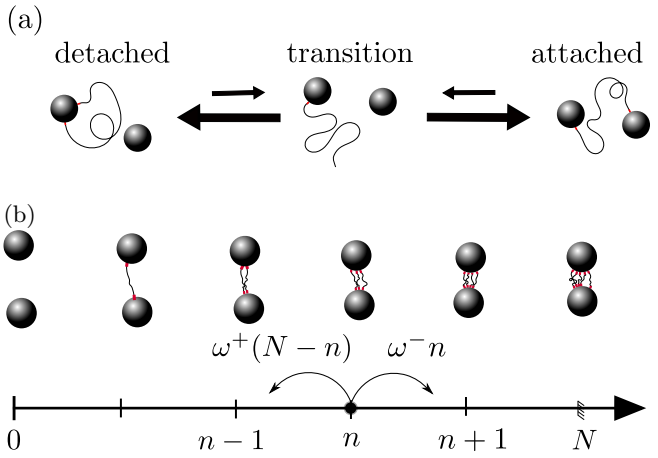


FIG. 2. We model superbond breaking as the disconnection of many independent polymer strands. (a) Disconnecting a single polymer strand requires going through a high-energy, short-lived transition state (larger arrows indicate faster transitions). The detached and attached states both have two polymer-crosslinker bonds, and therefore have the same energy. (b) Individual strands in a superbond attach and detach independently, resulting in a one-dimensional random walk in the number $n$ of attached strands [Eq. (3)]. Detached strands are not drawn here.

$$\begin{aligned}\partial_t P_n(t) =& \omega^+(N-n+1)P_{n-1}(t) + \omega^-(n+1)P_{n+1}(t) \\ &- [\omega^+(N-n) + \omega^- n]P_n(t),\end{aligned} \tag{3}$$

which ensures that the number of bound polymers can never be greater than $N$.

To determine the rate at which a superbond breaks, we set an absorbing boundary condition $P_0(t) = 0$ and define its survival probability as $S(t) = \sum_{n=1}^{N} P_n(t)$. In the limit $N \gg 1$ where a large number of strands are involved in the superbond, the detachment of the two beads is analogous to a Kramers escape problem. The average detachment time reads [27]

$$\tau_N \underset{N\to\infty}{\sim} \frac{\tau_0 e^{\beta\Delta E}}{N p_{\text{off}}^N} \tag{4}$$

and the survival probability decays as a single exponential $S(t) = \exp(-t/\tau_N)$ [28, 29]. The breaking of the superbond can thus be assimilated to a Poisson process with rate $1/\tau_N$ regardless of the initial condition $P_n(0)$.

Equation (4) implies a strong, exponential dependence of the average superbond breaking rate on the number $N$ of strands, implying that any polydispersity in this number may result in a wide distribution of time scales. Two factors influence the distribution of $N$. First, its value is constrained by the available space at the surface of each crosslinker, which we model by setting an upper

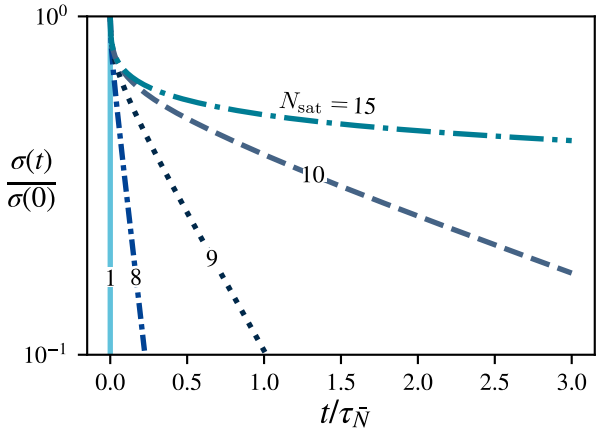


FIG. 3. Polydisperse, high-valence superbonds initially display a non-exponential mechanical relaxation, then cross over to an exponential regime when only the saturated superbonds remain. Curves plotted from Eq. (6) with $p_{\rm off}=0.2$, $\bar{N}=10$ and different values of $N_{\rm sat}$ as indicated on each curve.

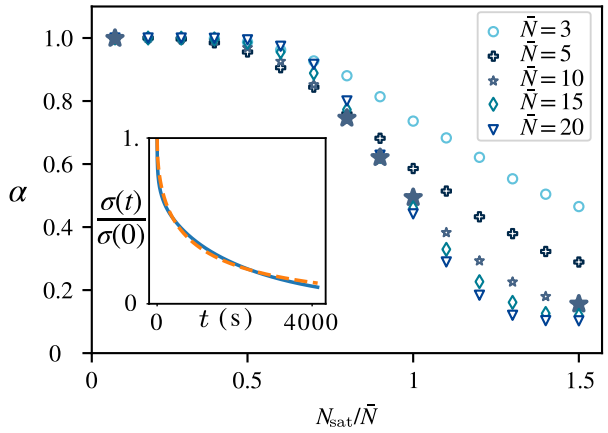


FIG. 4. Relationship between the stretched exponent $\alpha$ quantifying the non-exponential character of the relaxation and the microscopic parameter $N_{\rm sat}/\bar{N}$. Here $p_{\rm off}=0.2$. A low $N_{\rm sat}/\bar{N}$ gives an exponential relaxation ($\alpha\simeq 1$), while a larger $N_{\rm sat}/\bar{N}$ leads to a more complex behavior. While $\alpha$ appears to converge to a finite value for large $N_{\rm sat}/\bar{N}$ for the largest values of $\bar{N}$, this behavior is contingent on our choice of fitting interval. This issue does not affect the rest of the curves. Large stars correspond to the curves represented in Fig. 3. Inset: illustration of the quality of the fits between the heuristic stretched exponential [Eq. (1)] and our prediction [Eq. (6)].

bound $N_{\rm sat}$ on the number of polymer strands (attached and detached) participating in any superbond. Second, depending on the local density of polymer in the vicinity of the superbond, the actual number of strands present may be lower than $N_{\rm sat}$. Assuming that polymer strands are independently distributed throughout the system, the distribution of local strand concentrations within a small volume surrounding a superbond should be described by a Poisson distribution. We thus assume that $N$ is also described by a Poisson distribution up to its saturation at $N_{\rm sat}$:

$$p(N)=\begin{cases}\frac{\bar{N}^N e^{-\bar{N}}}{N!} & \text{for } N<N_{\rm sat}\\ \sum_{K=N_{\rm sat}}^{+\infty}\frac{\bar{N}^K e^{-\bar{N}}}{K!} & \text{for } N=N_{\rm sat}\end{cases}, \qquad (5)$$

where $\bar{N}$ would be the average number of strands in a superbond in the absence of saturation.

In response to a step strain, we assume that each superbond is stretched by an equal amount, and resists the step strain with an equal force before breaking. Superbonds may subsequently reform, but newly formed bonds are not preferentially stretched in the direction of the step strain and therefore do not contribute to the macroscopic stress on average. Denoting by $t=0$ the time at which the step strain is applied and by $\sigma(t)$ the resulting time-dependent shear stress, the progressive breaking of the initial superbonds results in the following stress response function:

$$\frac{\sigma(t)}{\sigma(t=0)}=\sum_{N=1}^{N_{\rm sat}}\frac{p(N)}{1-p(0)}e^{-t/\tau_N}. \qquad (6)$$

While the breaking times $\tau_N$ are unaffected by the applied stress in the linear response regime, nonlinearities can easily be included in our formalism by making $\Delta S$ stress-dependent and thus favor strand detachment. The relaxation described in Eq. (6) occurs in two stages. At long times $t\gg\tau_{N_{\rm sat}}$, few short-lived superbonds remain. Saturated superbonds ($N=N_{\rm sat}$) dominate the response and Eq. (6) is dominated by the last term of its sum. As a result the stress relaxes exponentially over time, as seen from the linearity of the curves of Fig. 3 for large values of $t$. Systems with smaller values of $N_{\rm sat}$ manifest this regime at earlier times; in the most extreme case, the relaxation of a system where superbonds involve at most a single polymer strand ($N_{\rm sat}=1$) is fully exponential and extremely fast as compared to systems with higher $N_{\rm sat}$. Over short times ($t\ll\tau_{N_{\rm sat}}$), stress relaxation involves multiple time scales. This non-exponential regime is apparent on the left of Fig. 3.

While Eq. (6) is not identical to the stretched exponential of Eq. (1), the inset of Fig. 4 shows that they are remarkably close in practice. We thus relate the stretched exponent $\alpha$ to the saturation number $N_{\rm sat}$ by fitting the stretched exponential to our predicted stress response function over the time interval required to relax 90% of the initial stress (Fig. 4). The fits are very close matches, and consistently give correlation factors $r^2>0.98$ (see detailed plots in Ref. [29]). If $N_{\rm sat}\lesssim 0.5\bar{N}$ then $\alpha\simeq 1$, indicating a nearly-exponential relaxation. Indeed, in that case superbond saturation occurs well before the peak of the Poisson distribution of $N$. Physically, this implies that the local polymer concentration surrounding most superbonds is sufficient to saturate them. As almost all superbonds are saturated, they decay over the same time scale $\tau_{N_{\rm sat}}$. As a result, the material as

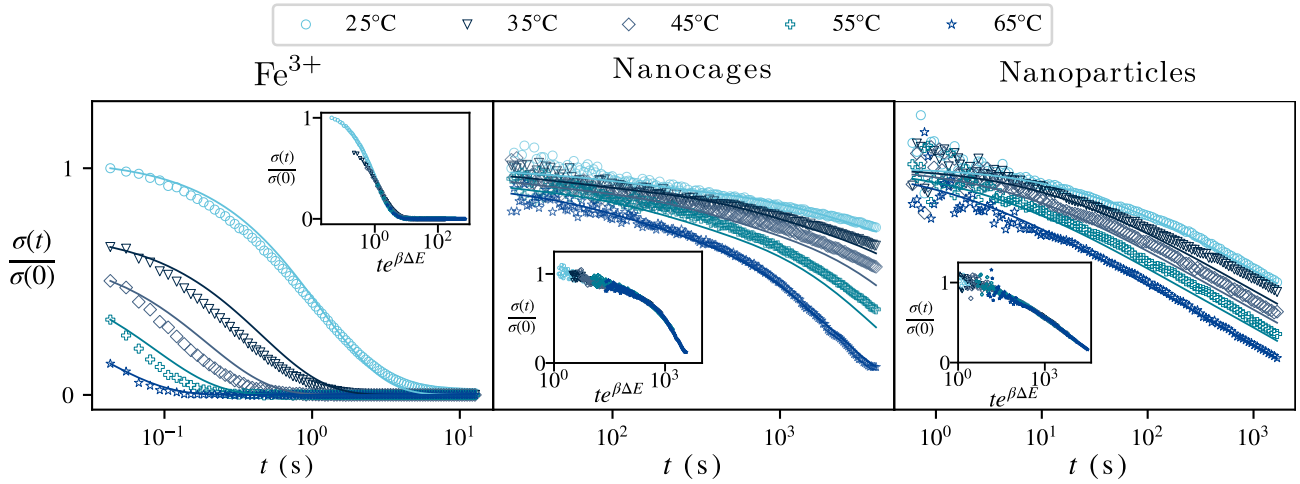


FIG. 5. Stress relaxation function for three experimental systems with increasing crosslinker valencies. Here we use a log-lin scale (unlike in Fig. 3) to facilitate the visualization a large range of time scales. Alternate representations are shown in Ref. [29]. Symbols are experimental datapoints, and the lines are the associated fitting curves. Insets: time-temperature collapsed data obtained by a rescaling $t \to te^{\beta\Delta E}$.

a whole displays an exponential relaxation. For larger values of $N_{\rm sat}$, the Poisson distribution is less affected by the saturation and the dynamics is set by the successive decay of superbonds involving an increasing number of strands, implying lower values of $\alpha$. The larger the value of $\bar{N}$, the sharper the crossover between these two regimes.

To validate our analysis of the impact of crosslinker valence on hydrogel relaxation, we compare Eq. (6) to experimental measurements. We perform step-strain experiments on three gels all involving the same type of polyethyleneglycol-based polymer stands terminated by transient ligands, but whose crosslinkers cover a wide range of valencies (Fig. 5) [15]. The first system has nitrocatechol ligands crosslinked by single $Fe^{3+}$ ions, with an estimated valence of 3. In the second system, pyridine ligands bind together through $Pd^{2+}$ ions to self-assemble into nanocages that crosslink up to 14 strands [30]. The third and final system has nitrocatechol ligands crosslinked by iron nanoparticles with a mean diameter of 7 nm, implying a surface area that allows the simultaneously binding of $\simeq 80$ ligands. To estimate the value of $N_{\rm sat}$ associated with each system from these valencies, we reason that each crosslinker shares its strands between 6 nearest neighbors as in a cubic lattice, *i.e.*, $N_{\rm sat} = \text{valence}/6$ (Table I).

In our model, the detachment of a single polymer strand proceeds independent of its environment, implying the existence of a single energy scale $\Delta E$. As a result, all time scales involved in the relaxation are proportional to $\exp(-\beta\Delta E)$. We confirm this prediction through a time-temperature collapse (Fig. 5, insets; details in Ref. [29]), and indicate the corresponding value of $\Delta E$ for each system in Table I. The energy scales associated with our three systems are of the same order despite some chemical differences (including distinct ligands in nanocages, lower pH and different state of oxydation of the nanoparticles compared to the ions). These values are moreover in order-of-magnitude agreement with the $\Delta E = 36 k_B T$ Arrhenius energy measured by stopped flow for the unbinding of a single nitrocatechol from a nanoparticle-like surface [15].

To compare the temperature-collapsed curves to our prediction of Eq. (6), we round our $N_{\rm sat}$ estimates to integer values and fit the parameters $p_{\rm off}$, $\tau_0$ and $\bar{N}$ across multiple temperatures. The resulting fits (Fig. 5) show a good agreement between the theory and experiments across up to 4 orders of magnitude in time scales. The fitted values of $p_{\rm off}$ and the single strand unbinding time $\tau_1$ are consistent across all three system, consistent with their chemically similar yet not identical binding mech-

| **crosslinker** | $Fe^{3+}$ | nanocages | nanoparticles |
|---|---|---|---|
| **estimated valence** | 3 | 14 | 80 |
| **estimated $N_{\rm sat}$** | 0.5 | 2.33 | 13.33 |
| **rounded $N_{\rm sat}$** | 1 | 3 | 13 |
| **$\Delta E$** (units of $k_BT$) | 28 | 24 | 24 |
| **$p_{\rm off}$** | 0.05 | 0.03 | 0.31 |
| **$\tau_1$** at $T = 300\,$K (s) | 0.05 | 2.4 | 0.14 |
| **$\bar{N}$** | 1 | 4.1 | 10.4 |

TABLE I. Estimated and fitted parameters involved in the comparison between experiment and theory in Fig. 5. The energies are given in units of $k_BT$ for $T = 300\,$K. Instead of presenting the parameter $\tau_0$, we present the more easily interpreted unbinding time of a single polymer strand at $300K$, namely $\tau_1 = \tau_0 e^{\beta_{300}\Delta E}$.

anisms (Table I). These values are moreover consistent with previous measurements suggesting $\tau_1 \approx 1\,\mathrm{s}$ [15]. Finally, the values of $\bar{N}$ cover the range of scenarios discussed above: exponential relaxation ($\bar{N} = N_{\mathrm{sat}} = 1$ for $Fe^{3+}$), a complex relaxation soon followed by an exponential phase ($\bar{N} \simeq N_{\mathrm{sat}} > 1$ for nanocages), and an extended complex relaxation ($\bar{N} < N_{\mathrm{sat}}$ for nanoparticles).

Our model bears some similarity with standard random energy trap models [31]. There, a long-tailed relaxation emerges from a short-tailed distribution of trap depths due to the exponential dependence of the relaxation times on the trap depths. Similarly, here a nonexponential relaxation emerges from a short-tailed distribution of superbond sizes $N$ [Eq. (5)] thanks to the exponential dependence of $\tau_N$ on $N$ [Eq. (4)]. In contrast with trap models however, our model does not predict a glass transition upon a lowering of temperature. It instead displays a simple Arrhenius time-temperature relation, consistent with the experimental collapses in the insets of Fig. (5). A crucial additional benefit of our approach is the direct connection between the predicted relaxation and experimentally accessible parameters such as the polymer concentration (through $\bar{N}$) or the nanoparticle area (through $N_{\mathrm{sat}}$). Our model can also account for the power-law relaxation observed in many rheological system [17–19] provided Eq. (5) is replaced by $p(N) \propto \exp(-N/\bar{N})$. This yields [29]

$$\frac{\sigma(t)}{\sigma(0)} \propto t^{1/\bar{N}\ln(p_{\mathrm{off}})}, \tag{7}$$

up to logarithmic corrections, which explicitly links the exponent of the power law to the parameters of the microscopic model. As the distribution of $N$ is borne out of the heterogeneity of the system, our model suggests a possible control of the system's rheology through $p(N)$. This distribution could in turn be modulated through the spatial distribution of the polymer strands and the polydispersity of the crosslinkers. Our model can further be used to predict the frequency dependence of the storage and loss moduli in a small oscillatory strain experiment, and again predicts power law regimes when $p(N)$ is exponential [29]. It can also easily be extended into the nonlinear response regime by introducing a stress-dependence of the strand attachment probability $p_{\mathrm{off}}$.

Our model reproduces several qualitative characteristics of the rheology of multivalent hydrogels, such as the strong influence of the crosslinker valence, Arrhenius temperature dependence and the transition between a nonexponential and an exponential regime at long times. Due to its simple, widely applicable microscopic assumptions we believe that it could help shed light on a wide range of multivalent systems. Beyond composite gels, it could thus apply to RNA-protein biocondensates where multivalent interactions between proteins are mediated by RNA strands [32], as well as cytoskeletal systems where filaments linked to many other filaments display a slow relaxation reminiscent of that of our multivalent crosslinkers [33].


[1] Olivier Ronsin, C Caroli, and Tristan Baumberger. Glass-like dynamics of the strain-induced coil/helix transition on a permanent polymer network. *The Journal of chemical physics*, 144(6):064904, 2016.

[2] Ana C Borges, Christian Eyholzer, Fabien Duc, Pierre-Etienne Bourban, Philippe Tingaut, Tanja Zimmermann, Dominique P Pioletti, and Jan-Anders E Månson. Nanofibrillated cellulose composite hydrogel for the replacement of the nucleus pulposus. *Acta biomaterialia*, 7(9):3412–3421, 2011.

[3] Ovijit Chaudhuri, Luo Gu, Max Darnell, Darinka Klumpers, Sidi A Bencherif, James C Weaver, Nathaniel Huebsch, and David J Mooney. Substrate stress relaxation regulates cell spreading. *Nature communications*, 6(1):1–7, 2015.

[4] Davoud Mozhdehi, James A Neal, Scott C Grindy, Yves Cordeau, Sergio Ayala, Niels Holten-Andersen, and Zhibin Guan. Tuning dynamic mechanical response in metallopolymer networks through simultaneous control of structural and temporal properties of the networks. *Macromolecules*, 49(17):6310–6321, 2016.

[5] Michael P Howard, Zachary M Sherman, Adithya N Sreenivasan, Stephanie A Valenzuela, Eric V Anslyn, Delia J Milliron, and Thomas M Truskett. Effects of linker flexibility on phase behavior and structure of linked colloidal gels. *The Journal of Chemical Physics*, 154(7):074901, 2021.

[6] Arti Vashist, Ajeet Kaushik, Anujit Ghosal, Jyoti Bala, Roozbeh Nikkhah-Moshaie, Waseem A Wani, Pandiaraj Manickam, and Madhavan Nair. Nanocomposite hydrogels: advances in nanofillers used for nanomedicine. *Gels*, 4(3):75, 2018.

[7] Qigang Wang, Justin L Mynar, Masaru Yoshida, Eunji Lee, Myongsoo Lee, Kou Okuro, Kazushi Kinbara, and Takuzo Aida. High-water-content mouldable hydrogels by mixing clay and a dendritic molecular binder. *Nature*, 463(7279):339–343, 2010.

[8] Tirtha Chatterjee, Alan I. Nakatani, and Antony K. Van Dyk. Shear dependent interactions in hydrophobically modified ethylene oxide urethane (heur) based rheology modifier latex suspensions: Part 1. molecular microstructure. *Macromolecules*, 2014.

[9] Niels Holten-Andersen, Matthew J Harrington, Henrik Birkedal, Bruce P Lee, Phillip B Messersmith, Ka Yee C Lee, and J Herbert Waite. ph-induced metal-ligand cross-links inspired by mussel yield self-healing polymer networks with near-covalent elastic moduli. *Proceedings of the National Academy of Sciences*, 108(7):2651–2655, 2011.

[10] Shengtong Sun, Li-Bo Mao, Zhouyue Lei, Shu-Hong Yu, and Helmut Cölfen. Hydrogels from amorphous calcium carbonate and polyacrylic acid: bio-inspired materials for "mineral plastics". *Angewandte Chemie International Edition*, 55(39):11765–11769, 2016.

[11] Jun Fu. Strong and tough hydrogels crosslinked by multifunctional polymer colloids. *Journal of Polymer Science*

*Part B: Polymer Physics*, 56(19):1336–1350, 2018.

[12] M. N. Dominguez et. al. Assembly of linked nanocrystal colloids by reversible covalent bonds. *Chem Mater*, 2020.

[13] German Alberto Parada and Xuanhe Zhao. Ideal reversible polymer networks. *Soft Matter*, 14(25):5186–5196, 2018.

[14] Scott C Grindy, Robert Learsch, Davoud Mozhdehi, Jing Cheng, Devin G Barrett, Zhibin Guan, Phillip B Messersmith, and Niels Holten-Andersen. Control of hierarchical polymer mechanics with bioinspired metal-coordination dynamics. *Nature materials*, 14(12):1210–1216, 2015.

[15] Jake Song, Qiaochu Li, Hugo Le Roy, Aleksandr V. Zhukhovitskiy, Jeremiah A. Johnson, Martin Lenz, Gareth McKinley, and Niels Holten-Andersen. Engineering broad stress relaxation curves in associative polymer gels via multi-functional cross-linkers. *PrePrint*, 2021.

[16] Jean-Philippe Bouchaud. Anomalous relaxation in complex systems: from stretched to compressed exponentials. *Anomalous Transport*, pages 327–345, 2008.

[17] GW Scott Blair and Jonathan Burnett. On the creep, recovery, relaxation and elastic" memory" of some renneted milk gels. *British Journal of Applied Physics*, 10(1):15, 1959.

[18] Bavand Keshavarz, Thibaut Divoux, Sébastien Manneville, and Gareth H McKinley. Nonlinear viscoelasticity and generalized failure criterion for polymer gels. *ACS Macro Letters*, 6(7):663–667, 2017.

[19] Martial Balland, Nicolas Desprat, Delphine Icard, Sophie Féréol, Atef Asnacios, Julien Browaeys, Sylvie Hénon, and François Gallet. Power laws in microrheology experiments on living cells: Comparative analysis and modeling. *Physical Review E*, 74(2):021911, 2006.

[20] Richard G Palmer, Daniel L Stein, Elihu Abrahams, and Philip Warren Anderson. Models of hierarchically constrained dynamics for glassy relaxation. *Physical Review Letters*, 53(10):958, 1984.

[21] Yuval Mulla, FC MacKintosh, and Gijsje H Koenderink. Origin of slow stress relaxation in the cytoskeleton. *Physical Review Letters*, 122(21):218102, 2019.

[22] M E Cates and S J Candau. Statics and dynamics of worm-like surfactant micelles. *J. Phys.: Condens. Matter*, 2:6869, 1990.

[23] Alberto Gomez-Casado, Henk H Dam, M Deniz Yilmaz, Daniel Florea, Pascal Jonkheijm, and Jurriaan Huskens. Probing multivalent interactions in a synthetic host–guest complex by dynamic force spectroscopy. *Journal of the American Chemical Society*, 133(28):10849–10857, 2011.

[24] Cécile Monthus and Jean-Philippe Bouchaud. Models of traps and glass phenomenology. *PNAS*, 2010.

[25] Peter Sollich, François Lequeux, Pascal Hébraud, and Michael E. Cates. Rheology of soft glassy materials. *Physical Review Letter*, 1997.

[26] Fumihide Tanaka and Samuel Frederick Edwards. Viscoelastic properties of physically crosslinked networks: Part 1. non-linear stationary viscoelasticity. *Journal of Non-Newtonian Fluid Mechanics*, 43(2-3):247–271, 1992.

[27] Nicolaas Godfried VAN KAMPEN. *STOCHASTIC PROCESSES IN PHYSICS AND CHEMISTRY*. Elsevier, 2007.

[28] Christophe Texier. Individual energy level distributions for one-dimensional diagonal and off-diagonal disorder. *J. Phys. A Math. Gen.*, 33:6095–6128, 2000.

[29] supplementary material.

[30] Aleksandr V Zhukhovitskiy, Mingjiang Zhong, Eric G Keeler, Vladimir K Michaelis, Jessie EP Sun, Michael JA Hore, Darrin J Pochan, Robert G Griffin, Adam P Willard, and Jeremiah A Johnson. Highly branched and loop-rich gels via formation of metal–organic cages linked by polymers. *Nature chemistry*, 8(1):33–41, 2016.

[31] Jean-Philippe Bouchaud. Weak ergodicity breaking and aging in disordered systems. *Journal de Physique I*, 2(9):1705–1713, 1992.

[32] Jeong-Mo Choi, Alex S. Holehouse, and Rohit V. Pappu. Physical Principles Underlying the Complex Biology of Intracellular Phase Transitions. *Annual Review of Biophysics*, 49(1):107–133, 2020.

[33] O. Lieleg, J. Kayser, G. Brambilla, L. Cipelletti, and A. R. Bausch. Slow dynamics and internal stress relaxation in bundled cytoskeletal networks. *Nature Materials*, 10(3):236–242, March 2011.

# Supplementary material
# Valence can control the non-exponential viscoelastic relaxation of reversible multivalent gels

Hugo Le Roy,[1,*] Jake Song,[2] Gareth H. McKinley,[3] Niels Holten-Andersen,[2] and Martin Lenz[1,4,†]

[1] *Université Paris-Saclay, CNRS, LPTMS, 91405, Orsay, France*
[2] *Department of Materials Science and Engineering, Massachusetts Institute of Technology, 77 Massachusetts Avenue, Cambridge, MA 02139, USA*
[3] *Department of Mechanical Engineering, Massachusetts Institute of Technology, 77 Massachusetts Avenue, Cambridge, MA 02139, USA*
[4] *PMMH, CNRS, ESPCI Paris, PSL University, Sorbonne Université, Université de Paris, F-75005, Paris, France*



## I. DISTRIBUTION OF SUPERBOND BREAKING TIME AND DERIVATION OF $\tau_N$

Here we show that the survival probability for the detachment of a superbond (illustrated in main text Fig. 2) containing many polymer strands ($N \to \infty$) asymptotically goes to $S(t) = e^{-t/\tau_N}$, where $\tau_N$ is given by Eq. (4) of the main text. We first consider a general one-step process and derive the basic recursion equation used throughout the proof in Sec. I.1. We solve the recursion in Sec. I.2 and express the generating function of $S(t)$ as a double sum. In Sec. I.3, we apply the resulting formula to our particular problem and take the continuum limit of the second sum. Finally, we compute both sums in the $N \to \infty$ limit in Sec. I.4. Our derivation is adapted from the calculation presented in the appendix of Ref. [1].

### I.1. Backward Kolmogorov equation for the generating function of $S$

We consider a one-step process, *i.e.*, a stochastic process consisting of transitions between discrete states on a line, with transition rates $r_n$ and $g_n$ illustrated in Fig. S1(a). We denote the probability for the particle to be in state $k$ at time $t$ after starting in state $n$ at time 0 by $P(k,t|n)$. We assume an absorbing boundary condition in 0 and a reflecting boundary condition in $N$, *i.e.*,

$$\forall n \in [1..N] \quad P(0,t|n) = 0, \qquad r_N = 0. \tag{S1}$$

The backward Kolmogorov equation for our process reads [2]

$$\frac{\mathrm{d}P}{\mathrm{d}t}(k,t|n) = g_n[P(k,t|n+1) - P(k,t|n)] - r_n[P(k,t|n) - P(k,t|n-1)]. \tag{S2}$$

We define the survival probability and its generating function (Laplace transform), respectively as

$$S_n(t) = \sum_{k=1}^{N} P(k,t|n), \quad h_n(\alpha) = \int_0^{+\infty} S_n(t) e^{-\alpha t}\,\mathrm{d}t. \tag{S3}$$

Inserting these definitions into Eq. (S2) yields

$$\alpha h_n(\alpha) - 1 = g_n[h_{n+1}(\alpha) - h_n(\alpha)] - r_n[h_n(\alpha) - h_{n-1}(\alpha)], \tag{S4}$$

which we endeavor to solve for $h_n(\alpha)$ in the following.

* hugo.le-roy@universite-paris-saclay.fr
† martin.lenz@universite-paris-saclay.fr

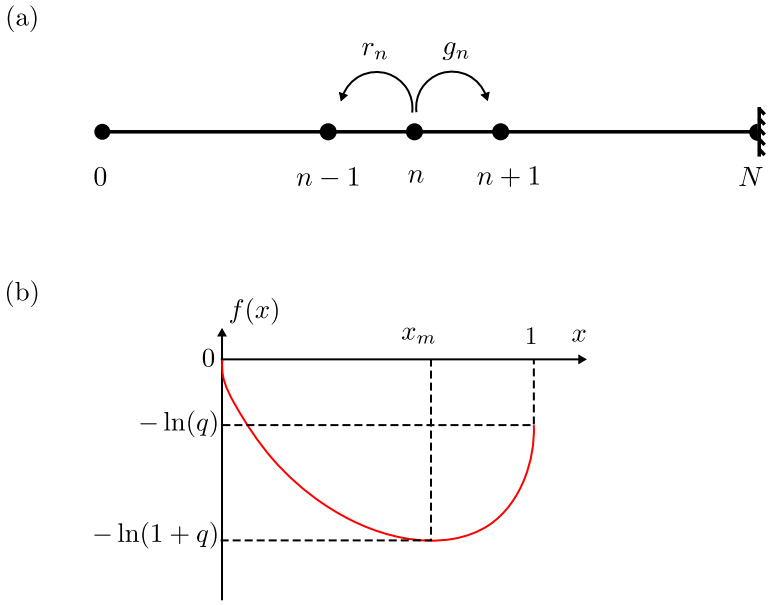


FIG. S1. Superbond detachment as a Kramers-like barrier-crossing problem. (a) Definition of the rates of the one-step process. (b) Profile of the pseudo-free energy defined in Eq. (S13). Superbond detachment requires the system to fluctuate out of the free energy well to the $x = 0$ absorbing state, with $1/N$ playing the role of a temperature.

### I.2. Sum equation for the generating function

We define a rescaled current between sites $n-1$ and $n$

$$\Delta_n = \begin{cases} r_n \left( \prod_{i=n}^{N-1} \frac{r_{i+1}}{g_i} \right) [h_n - h_{n-1}] & \text{for } n < N \\ r_N [h_N - h_{N-1}] & \text{for } n = N \end{cases}. \tag{S5}$$

This allows us to turn the two-step recursion of Eq. (S4) into one with only one step:

$$\Delta_n = \begin{cases} \Delta_{n+1} + \left( \prod_{i=n}^{N-1} \frac{r_{i+1}}{g_i} \right) [1 - \alpha h_n] & \text{for } n < N \\ 1 - \alpha h_N & \text{for } n = N \end{cases}, \tag{S6}$$

which can easily be summed as

$$\Delta_n = \left[ \sum_{j=n}^{N-1} \left( \prod_{i=n}^{N-1} \frac{r_{i+1}}{g_i} \right) (1 - \alpha h_j) \right] + 1 - \alpha h_N. \tag{S7}$$

We now invert Eq. (S5) and use Eq. (S7) to express the finite difference $(h_n - h_{n-1})$. We further use the property that $h_m = h_0 + \sum_{n=1}^{m} (h_n - h_{n-1})$ and recognize that $h_0 = 0$ due to Eq. (S1) to obtain

$$h_m = \sum_{n=1}^{m} \frac{1}{r_N} \left( \prod_{i=n}^{N-1} \frac{g_i}{r_{i+1}} \right) \left\{ \left[ \sum_{j=n}^{N-1} \left( \prod_{i=n}^{N-1} \frac{r_{i+1}}{g_i} \right) (1 - \alpha h_j) \right] + 1 - \alpha h_N \right\}. \tag{S8}$$

### I.3. Application and continuum limit

Using the mean detachment time of a polymer strand (denoted as $\omega_-$ in the main text) as our unit of time and defining $q = \omega_+/\omega_-$, the model of the main text implies

$$\forall n \in [1..N] \quad r_n = n, \quad g_n = (N-n)q, \tag{S9}$$

which we insert into Eq. (S8) to obtain

$$h_n = \sum_{j=1}^{n} \frac{1}{j\binom{N}{j}q^j} \sum_{i=j}^{N} \binom{N}{i} q^i (1 - \alpha h_i). \tag{S10}$$

In Eq. (S10), the outermost sum is dominated by the very small values of $j$ in the limit $N \to \infty$. We thus need only consider small values of $j$ when computing the innermost sum, which happens to be dominated by a value of $i$ far from the edges of the $[1..N]$ interval. We can thus take its continuum limit. Using Stirling's formula, we obtain

$$h_n \underset{N\to\infty}{\sim} \sum_{j=1}^{n} \frac{1}{j\binom{N}{j}q^j} \int_0^1 \sqrt{\frac{N}{2\pi x(1-x)}} e^{-Nf(x)} [1 - \alpha h(x, \alpha)] \, \mathrm{d}x, \tag{S11}$$

where we have defined the continuum version of our generating function though $h(x, \alpha) = h_{Nx}(\alpha)$, as well as the pseudo free energy of the system

$$f(x) = x \ln x + (1 - x) \ln(1 - x) - x \ln q. \tag{S12}$$

This free energy has a single minimum in $x_m = q/(1 + q)$ with a locally parabolic structure given by

$$f(x) = -\ln(1 + q) + \frac{(1 + q)^2}{2q}(x - x_m)^2 + \mathcal{O}(x - x_m)^3, \tag{S13}$$

which we illustrate in Fig. S1(b). The problem at hand is exactly analogous to a Kramers escape problem from the bottom of this minimum to the $n = 0$ boundary condition, with $N \to \infty$ playing the role of the low-temperature limit.

### I.4. Asymptotic simplifications

Using the Kramers analogy to our advantage, we compute the integral of Eq. (S11) using a saddle-point approximation. We thus find that for any $x \in ]0, 1[$:

$$h(x, \alpha) \underset{N\to\infty}{\sim} (1 + q)^N [1 - \alpha h(x_m, \alpha)] \sum_{j=1}^{Nx} \frac{q^{-j}}{j\binom{N}{j}}. \tag{S14}$$

Using Stirling's formula for small values of $j$ reveals that the argument of the sum in Eq. (S14) goes as $(j-1)! \times (Nq)^{-j}$. Therefore, the terms of the sum are simply the terms in an expansion in powers of $N$. We keep only the lowest-order term to find

$$\forall x \in ]0, 1[ \quad h(x, \alpha) \underset{N\to\infty}{\sim} \tau_N [1 - \alpha h(x_m, \alpha)]. \tag{S15}$$

where

$$\tau_N = \frac{(1 + q)^N}{Nq} \tag{S16}$$

is the dimensionless version of the mean first-passage time presented in Eq. (4) of the main text.

Setting $x = x_m$, Eq. (S15) implies

$$h(x_m, \alpha) \underset{N\to\infty}{\sim} \frac{1}{\alpha + \tau_N^{-1}} \quad \Leftrightarrow \quad S_{Nx_m}(t) \underset{N\to\infty}{\sim} e^{-t/\tau_N}. \tag{S17}$$

Finally, using Eq. (S15) again yields

$$\forall x \in ]0, 1[ \quad S_{Nx}(t) \underset{N\to\infty}{\sim} -\tau_N \frac{\mathrm{d}S_{Nx_m}}{\mathrm{d}t}(t) = e^{-t/\tau_N}, \tag{S18}$$

which is the exponential distribution presented in the main text.

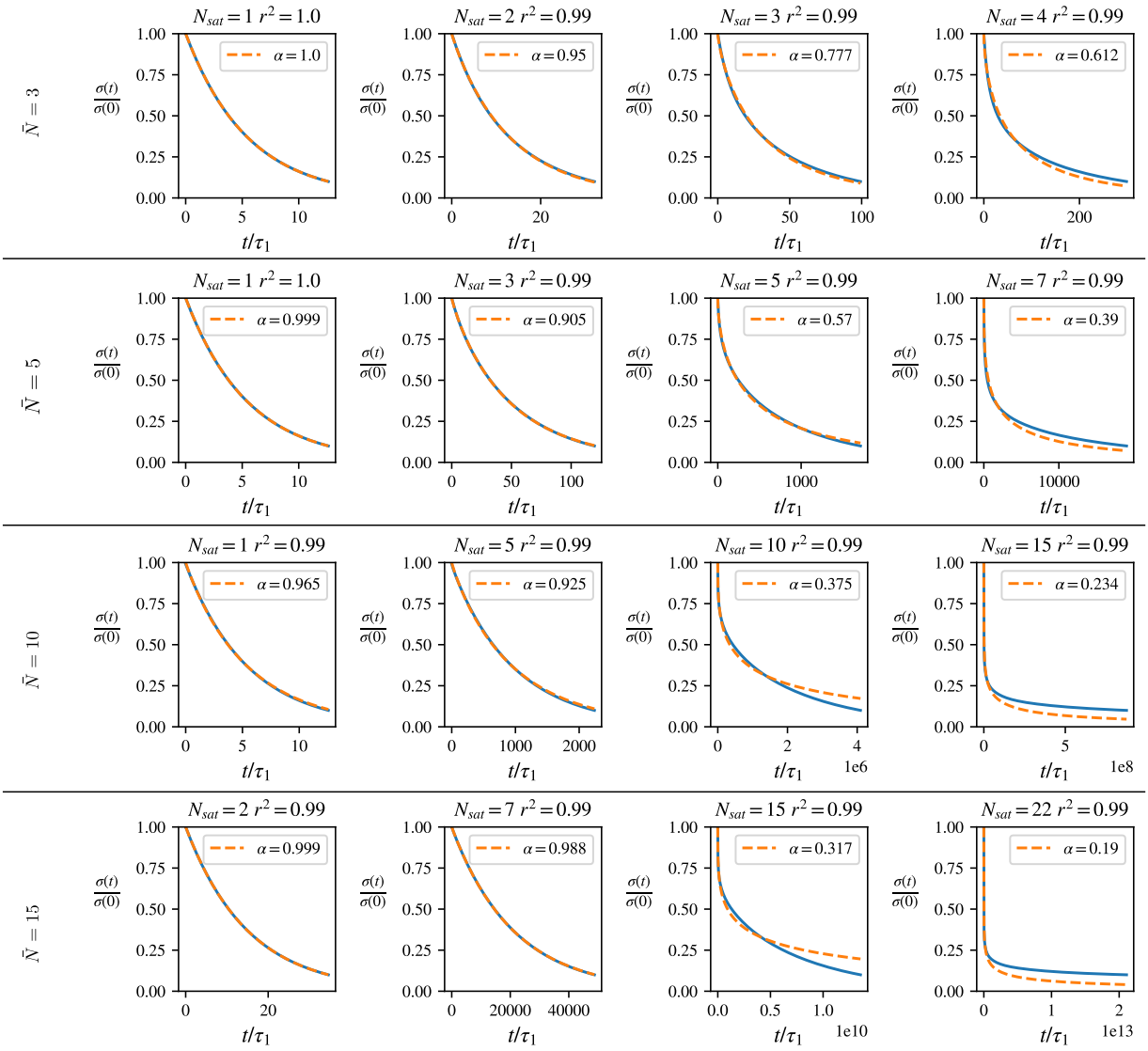


FIG. S2. Illustration of the similarity of our modeled stress response function with a stretched exponential. We plot the relaxation modulus computed using Eq. (6) of the main text for $\bar{N} \in [3, 5, 10, 15]$. For each value of $\bar{N}$, we plot four values of $N_{\rm sat}$, namely $N_{\rm sat} = 0.1\bar{N}$, $0.5\bar{N}$, $\bar{N}$ and $1.5\bar{N}$, $p_{\rm off} = 0.2$. Each plot also mentions the value of the stretch exponent $\alpha$ and the correlation coefficient $r^2$.

## II. LINK BETWEEN $\alpha$ AND $N_{\rm sat}/\bar{N}$

Here establish the connection between the stretch exponent $\alpha$ and the values of $N_{\rm sat}/\bar{N}$ shown in Fig. 4 of the main text. To mimic the observation of an experimental step strain over a finite time window, we focus our attention on the time interval between $t = 0$ and $t = \tau_{90}$, where $\tau_{90}$ is the time required to relax 90% of the stress, *i.e.*, $\sigma(\tau_{90}) = 0.1 \times \sigma(0)$. We plot the relaxation curve given by Eq. (6) of the main text over this time window, then perform a least-squares fit using a stretched exponential [Eq. (1) of the main text] with $\alpha$ and $\tau$ as fitting parameters. As shown in Fig. S2, the agreement is excellent over all parameters used. The corresponding value of the fitting parameters ($\tau$ and $\alpha$) for a broader variety of $\bar{N}$ and $N_{\rm sat}$ is also provided in Fig. S3. This suggests that experimental curves that are well fitted by a stretched exponential could be equally well described by our model.

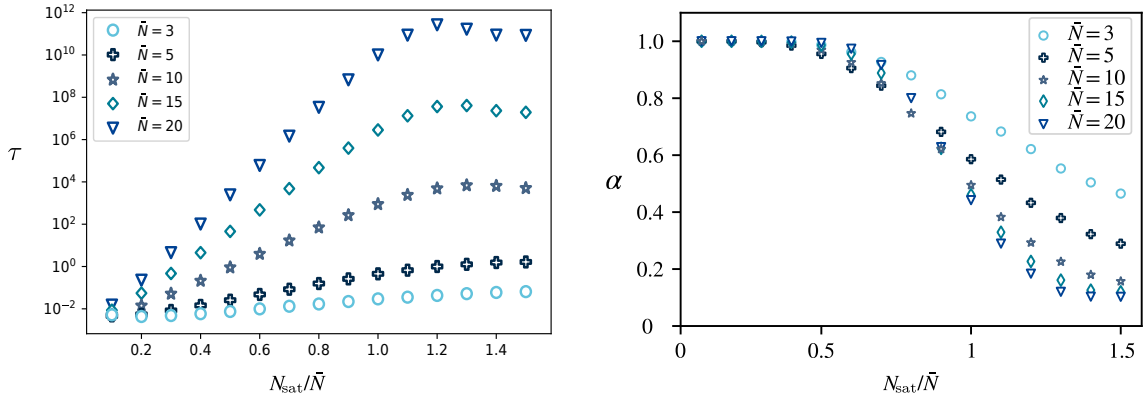


FIG. S3. Best fit values of the stretched exponential parameters $\tau$ and $\alpha$ for a range of values of $\bar{N}$ and $N_{\rm sat}$. The right-hand-side panel is identical to Fig. 4 of the main text.

## III. TIME-TEMPERATURE COLLAPSE

Here we describe the procedure used to determine the binding energy $\Delta E$ in the three experimental systems discussed in the main text. Equation (4) of the main text implies that the temperature dependence of the stress response function can be eliminated by expressing it as a function of the rescaled time $\tilde{t} = te^{\beta\Delta E}$. This should cause the relaxation curves of a given system at different temperatures to collapse.

For each type of ligand, we have 5 datasets showing the stress relaxation function as a function of time at each different temperature $\{T^{(\alpha)}\}_{\alpha\in[0,4]} = \{25°\text{C}, 35°\text{C}, 45°\text{C}, 55°\text{C}, 65°\text{C}\}$. To enable the comparison between time-rescaled datasets, we first define an interpolating function for the stress relaxation function at each temperature used. We thus compute the set of interpolating coefficients $\left\{p_k^{(\alpha)}\right\}_k$ by perform a least-square fit of the following rational function

$$P^{(\alpha)}(t) = \sum_{k=-3}^{10} p_k^{(\alpha)} t^k, \tag{S19}$$

to the datapoints $\left\{t_i^{(\alpha)}, \frac{\sigma^{(\alpha)}(t_i)}{\sigma^{(\alpha)}(0)}\right\}_i$. We furthermore define the interval of definition of $P^{(\alpha)}(x)$ as the range over which data is available, *i.e.*, $I_{P^{(\alpha)}} = \left[0, \max_i t_i^{(\alpha)}\right]$.

We then perform the collapse of the $\{T^{(\alpha)}\}_{\alpha\in[1,4]}$ interpolated curves onto the $T^{(0)}$ curve. To this effect we define the set of rescaling coefficients $\{a^{(\alpha)}\}_{\alpha\in[1,4]}$ and performs a separate time rescaling for each temperature: $\tilde{t} = te^{a^{(\alpha)}}$. For each $\alpha \in [1,4]$, we optimise the semidistance

$$D(P,Q) = \int_{I_Q\cap I_P} [P(t) - Q(t)]^2 \mathrm{d}t, \tag{S20}$$

between the functions $t \to P^{(0)}(t)$ and $t \to P^{(\alpha)}(te^{a^{(\alpha)}})$ with respect to $a^{(\alpha)}$. The resulting collapsed curves are shown in Fig. S4 (a,b,c). The optimal rescaling coefficients are plotted as a function of the inverse temperature $1/k_BT$ in Fig. S4 (d,e,f). Consistent with the time-temperature collapse hypothesis, this dependence is affine, and we use the slope of the best fitting line as our value of the binding energy $\Delta E$.

## IV. FIT OF THE STRESS RELAXATION FUNCTION TO OUR THEORETICAL PREDICTION

In the main text, we fit the experimental curves with the stress relaxation function predicted by our model. We then represent them on a log-lin scale to allow the simultaneous visualization of short and long time scales. In Fig. S5 we replot these curves in a lin-lin-scale, as well as a lin-log scale that emphasizes intervals of exponential relaxation as straight lines.

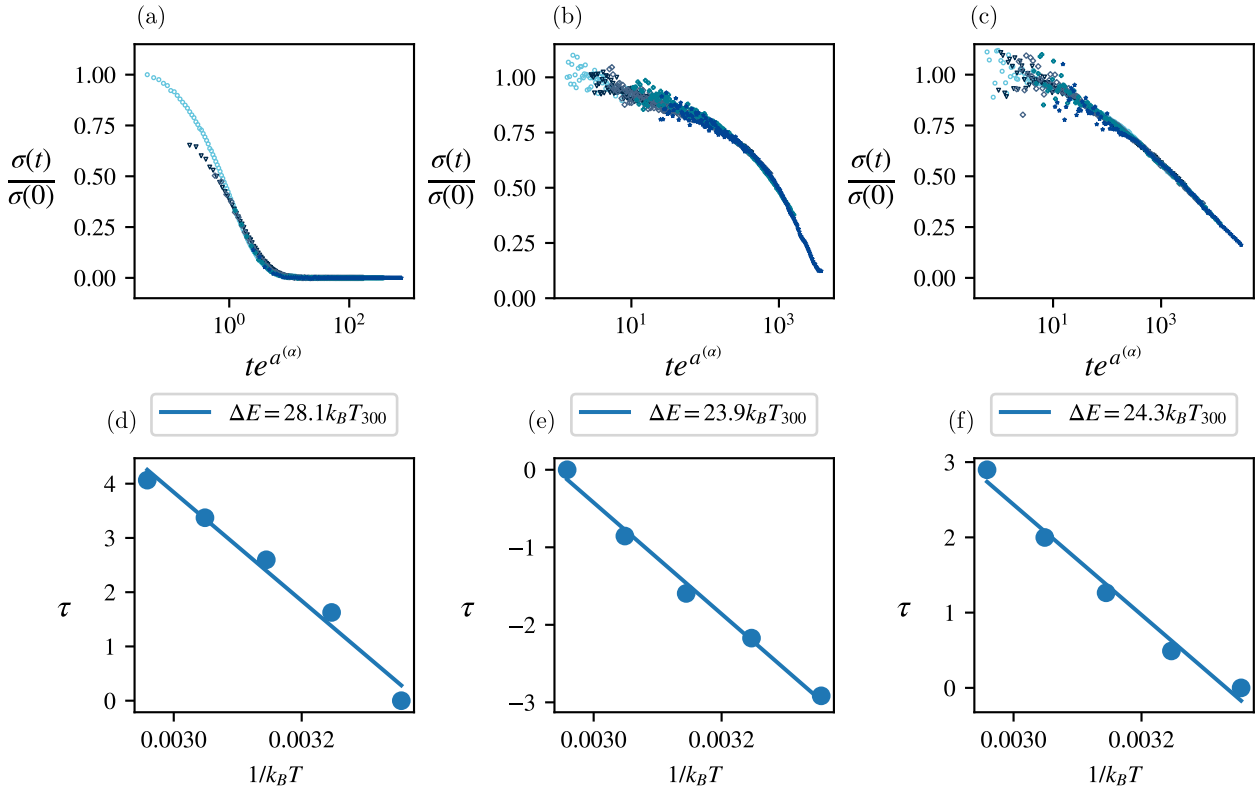


FIG. S4. **Collapse of the relaxation modulus:** (a-c) respectively the collapsed relaxation modulus of $Fe^{3+}$, nanocages, nanoparticles after the rescaling of the time for an optimized collapse. The curves are represented on a semilogarithmique axis, but the collapsing procedure is perfomed on a lin-lin scale. (d-f) corresponding rescaling parameters as a function of $1/(k_B T)$ the inverse temperature. The slope of the line is $-\Delta E$ and the legend gives the value of $\Delta E$ in $k_B T$ unit at $300K$.

## V. RATIONALIZATION OF THE POISSON DISTRIBUTION OF THE SUPERBOND SIZE $p(N)$

The polymers used in our experiments are 4-arms polyethylene glycol (PEG). At the end of each arm is a nitrocatechol ligand that allows crosslinker binding. In our model, we assume that the ends of a polymer are always attached to a ligand. For this reason, the diffusion of such a polymer over a distance comparable to the polymer size occurs on a time scale comparable to the time required to rearrange the bonds between crosslinkers, which corresponds to the time required for the relaxation of the stress in the system. Let us consider that the 4-arm PEG are able to diffuse over a volume $v$ during the time of the experiment.We model the spreading of the polymers in the system by discretizing the system into small boxes of volume $v$ between which no polymer exchange occurs over the duration of the experiment. As a result the distribution of the polymers over the boxes is due to the initial preparation of the system. We assume that this processes places each polymer in a random box with equal probability. As a result, the probability that a specific box contains $n$ polymers is given by a Poisson distribution:

$$P(n) = e^{-\rho_{\mathrm{PEG}} v} \frac{(\rho_{\mathrm{PEG}} v)^n}{n!}, \tag{S21}$$

where $\rho_{\mathrm{PEG}}$ is the average concentration of PEG in the system, and $v\rho_{\mathrm{PEG}}$ is the mean (over the system) number of $PEG$ in a box of volume $v$. Equation (S21) is the basis for Eq. (5) of the main text.

## VI. OUR MODEL CAN DESCRIBE A POWER LAW RELAXATION

As discussed in the main text, substituting the superbond size distribution Eq. (5) of the main text for an exponential distribution

$$p(N) = \left(1 - e^{-1/\bar{N}}\right) e^{-N/\bar{N}} \tag{S22}$$

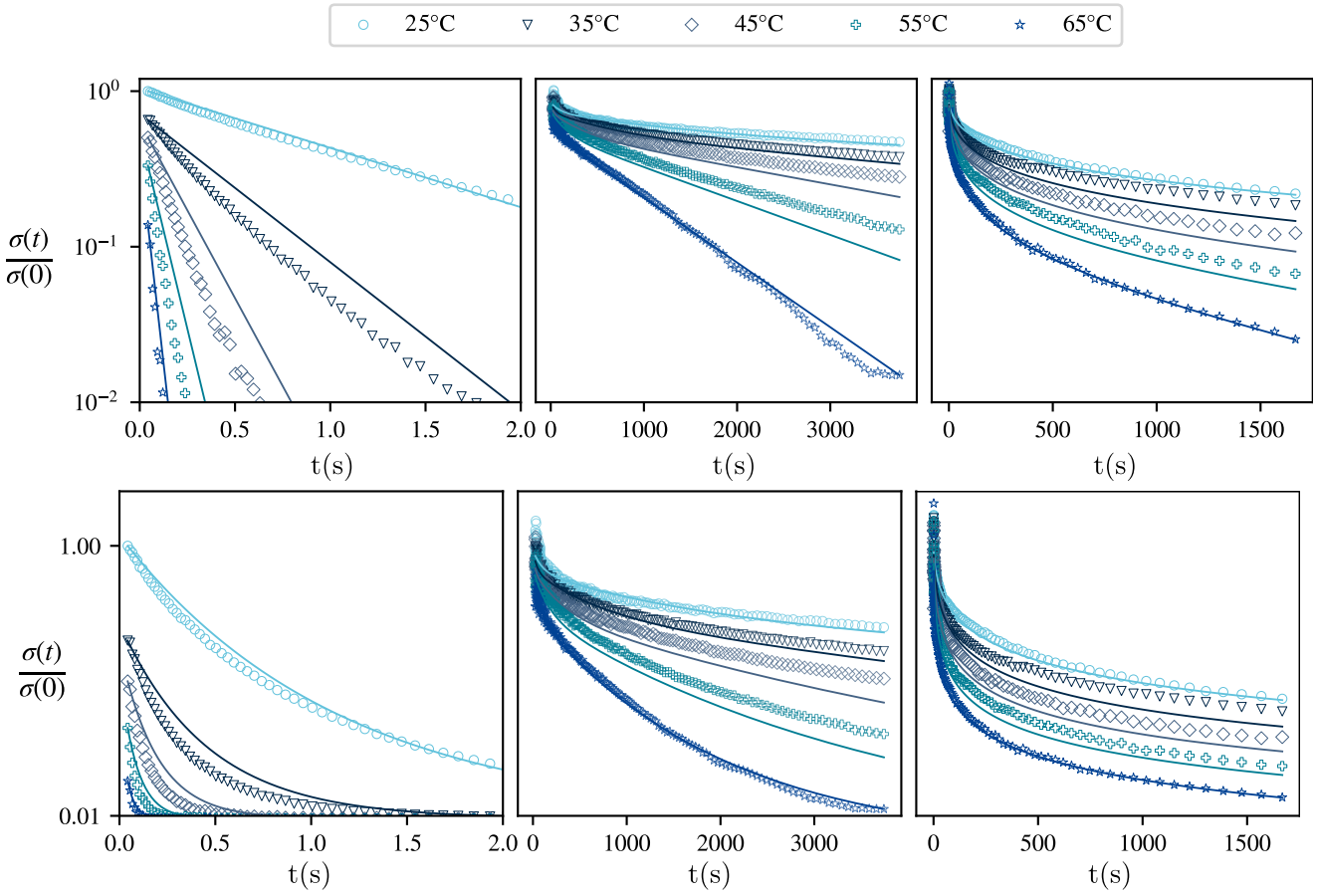


FIG. S5. Fits of the experimental curves : respectively lin-lin and lin-log representation of Fig. 5 in the main text.

yields a power-law relaxation regime provided that $\bar{N} \gg 1$, as shown in Fig. S6. Here we compute the value of the relaxation exponent.

Since Eq. (S22) does not saturate at a finite $N = N_{\rm sat}$, Eq. (6) of the main text becomes

$$\frac{\sigma(t)}{\sigma(0)} = \sum_{N=1}^{+\infty} \frac{p(N)}{1-p(0)} e^{-t/\tau_N} \qquad \text{with} \qquad \tau_N = \frac{\tau_0 e^{\beta\Delta E}}{N p_{\rm off}^N}. \tag{S23}$$

As the main dependence of $\tau_N$ on $N$ is exponential, in the large-$\bar{N}$ limit replacing the factor of $N$ preceding $p_{\rm off}^N$ by the typical value $\bar{N}$ induces only a small (logarithmic) error. We thus approximate

$$\tau_N \simeq \frac{\tau_0 e^{\beta\Delta E}}{\bar{N} p_{\rm off}^N}, \tag{S24}$$

and also take the continuum limit of the sum of Eq. (S23). Defining the dimensionless time $\tilde{t} = t\bar{N}/\tau_0 e^{\beta\Delta E}$, this yields

$$\frac{\sigma(t)}{\sigma(0)} \underset{\bar{N}\gg 1}{\sim} \int_0^{+\infty} p(N) e^{-\tilde{t} p_{\rm off}^N} \, {\rm d}N. \tag{S25}$$

We next change our integration variable to $\tilde{\tau} = p_{\rm off}^N$ to find

$$\frac{\sigma(t)}{\sigma(0)} \underset{\bar{N}\gg 1}{\sim} \int_1^{+\infty} \gamma \tilde{\tau}^{-(1+\gamma)} e^{-\tilde{t}/\tilde{\tau}} \, {\rm d}\tau \underset{\bar{N}\gg 1, \tilde{t}\gg 1}{\sim} \Gamma(1+\gamma)\tilde{t}^{-\gamma}, \qquad \text{where} \qquad \gamma = -\frac{1}{\bar{N}\ln p_{\rm off}} > 0 \tag{S26}$$

and where $\Gamma$ denotes the gamma function. Equation (S26) implies the power law presented in Eq. (7) of the main text, and its accuracy at long times is confirmed by the plots of Fig. (S6). As discussed in the main text, here an

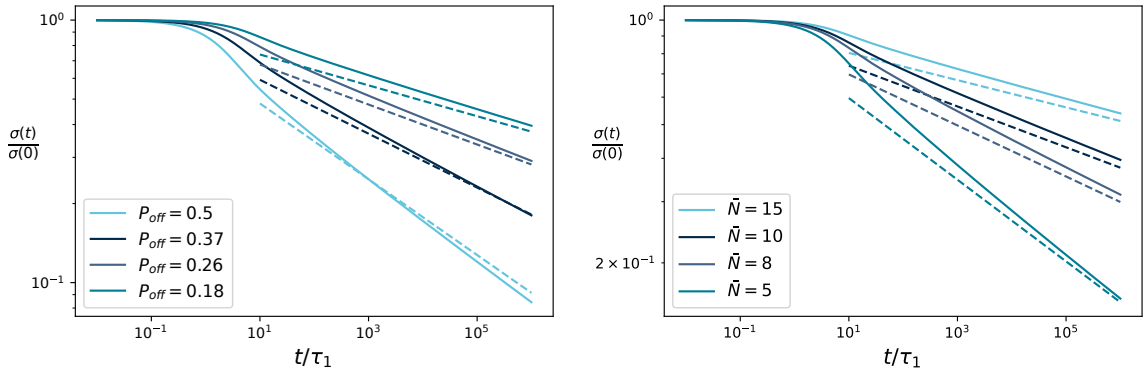


FIG. S6. Comparison between exact relaxation modulus of Eq. (S23) (solid lines) and the approximate expression of Eq. (S26) (dashed lines).

exponential distribution of $N$ combined with an exponential dependence of the relaxation time on $N$ [Eq. (S23)] result in a power law distribution of the relaxation times. This distribution is apparent in the integral on the left of Eq. (S26), and eventually results in the power law relaxation. Note that the approximation of Eq. (S24) leads us to ignore a possible logarithmic dependence of $\sigma(t) \times t^\gamma$ on $t$, hence the small mismatch between the curves of Fig. S6.

## VII. SCALING REGIMES FOR THE COMPLEX MODULUS

In the linear response regime, the Fourier transform of the stress is related to that of the strain $\epsilon$ through the material's complex modulus $G$:

$$\sigma(\omega) = G(\omega)\epsilon(\omega). \tag{S27}$$

Denoting the Heaviside step function by $H$, we consider the response to a step strain $\epsilon(t) = \epsilon_0 H(t)$ and thus obtain $\sigma(\omega)$ by Fourier transforming Eq. (S23). Eq. (S27) then yields

$$\int_0^{+\infty} e^{-i\omega t}\sigma(0) \sum_{N=1}^{N_{\text{sat}}} \frac{p(N)}{1-p(0)} e^{-t/\tau_N}\,\mathrm{d}t = G(\omega) \int_{-\infty}^{+\infty} e^{-i\omega t}\epsilon_0 H(t)\,\mathrm{d}t \tag{S28}$$

where the bounds of the left-hand-side integral stem from the implicit assumption that $\sigma(t < 0) = 0$ in Eq. (S23). We compute both integrals in Eq. (S28) to find

$$\tilde{G}(\omega) = \sum_{N=1}^{N_{\text{sat}}} \frac{p(N)}{1-p(0)} \frac{i\omega\tau_N}{1+i\omega\tau_N}, \tag{S29}$$

where $\tilde{G}$ is the dimensionless modulus obtained by normalizing $G$ by the high-frequency elastic plateau $\sigma(0)/\epsilon_0$.

In the following we consider a generalization of Eq. (S22) where $p(N) \propto \exp(-N/\bar{N})$ for $N \leq N_{\text{sat}}$ and $p(N) = 0$ for $N > N_{\text{sat}}$. We analyze the scaling behavior of the storage modulus $G'(\omega) = \Re[G(\omega)]$ and the loss modulus $G''(\omega) = \Im[G(\omega)]$ computed from Eq. (S29).

In the high-frequency regime $\omega \gg \tau_1^{-1}$, the system displays a Maxwell-like rheology:

$$\tilde{G}'(\omega) \underset{\tau_1^{-1} \ll \omega}{\sim} 1 \tag{S30a}$$

$$\tilde{G}''(\omega) \underset{\tau_1^{-1} \ll \omega}{\sim} \frac{e^{-1/\gamma\bar{N}}(1-e^{-1/\bar{N}})}{[1-e^{-(1+\gamma^{-1})/\bar{N}}]^2} \frac{1}{\omega\tau_1}. \tag{S30b}$$

We now consider the intermediate frequency regime $\tau_{N_{\text{sat}}}^{-1} \ll \omega \ll \tau_1^{-1}$ in the case $N_{\text{sat}} \gg 1$. Provided we also

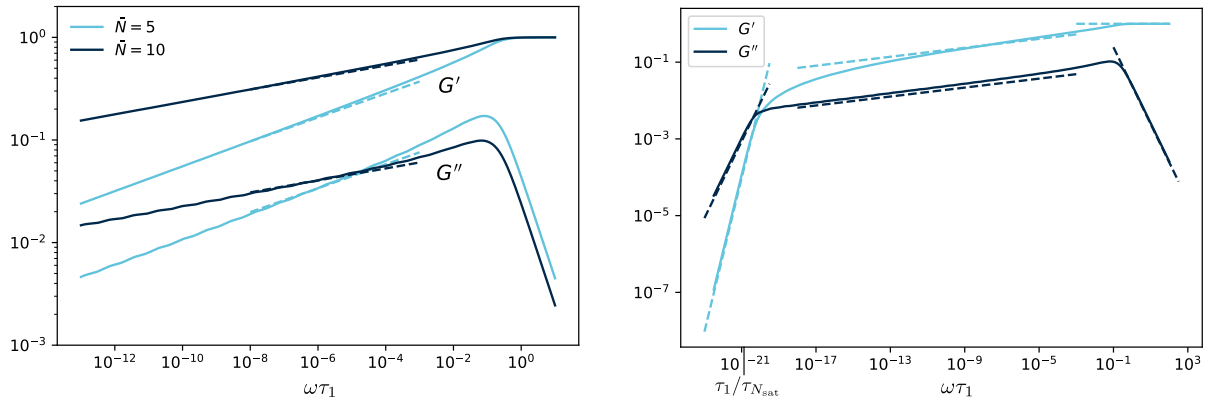


FIG. S7. Comparison between the storage and loss moduli computed from the exact expression Eq. (S29) (solid lines) and the asymptotic expressions of Eqs. (S30-S32) (dashed lines). We use $p_{\rm off} = 0.18$ throughout. *Left panel*: plots in the large $N_{\rm sat}$ limit ($N_{\rm sat} = 100$), showing a good agreement with the power law regime of Eq. (S31) for two values of $\bar{N}$ corresponding to $\gamma \simeq 0.116$ and $\gamma \simeq 0.0583$. *Right panel*: plots for a smaller value of $N_{\rm sat}$ ($N_{\rm sat} = 30$) showing the three distinct asymptotic regimes. Here $\bar{N} = 10 \Rightarrow \gamma \simeq 0.0583$. The marker at $\omega\tau_1 = \tau_1/\tau_{N_{\rm sat}}$ denotes the expected position of the low-frequency crossover, while the high-frequency crossover is expected for $\omega\tau_1 \approx 1$.

assume $1 \ll \bar{N} \ll N_{\rm sat}$, the approximate power law response of Eq. (S26) applies and we obtain

$$\tilde{G}'(\omega) \underset{\tau_{N_{\rm sat}}^{-1} \ll \omega \ll \tau_1^{-1}}{\sim} \begin{cases} \frac{\pi\gamma/2}{\sin(\pi\gamma/2)} e^{-1/\bar{N}} \left(\frac{\omega\tau_1}{\bar{N}}\right)^{\gamma} & \text{if } \gamma < 2 \\ \frac{\gamma}{\gamma-2} e^{-2/\gamma\bar{N}} \left(\frac{\omega\tau_1}{\bar{N}}\right)^{2} & \text{if } \gamma > 2 \end{cases} \tag{S31a}$$

$$\tilde{G}''(\omega) \underset{\tau_{N_{\rm sat}}^{-1} \ll \omega \ll \tau_1^{-1}}{\sim} \begin{cases} \frac{\pi\gamma/2}{\cos(\pi\gamma/2)} e^{-1/\bar{N}} \left(\frac{\omega\tau_1}{\bar{N}}\right)^{\gamma} & \text{if } \gamma < 1 \\ \frac{\gamma}{\gamma-1} e^{-1/\gamma\bar{N}} \left(\frac{\omega\tau_1}{\bar{N}}\right) & \text{if } \gamma > 1 \end{cases}. \tag{S31b}$$

Finally, at low frequencies $\omega \ll \tau_{N_{\rm sat}}^{-1}$, the system again goes to a Maxwell-like rheology:

$$\tilde{G}'(\omega) \underset{\omega \ll \tau_{N_{\rm sat}}^{-1}}{\sim} A(\gamma, \bar{N})(\omega\tau_1)^2 \tag{S32a}$$

$$\tilde{G}''(\omega) \underset{\omega \ll \tau_{N_{\rm sat}}^{-1}}{\sim} B(\gamma, \bar{N})(\omega\tau_1), \tag{S32b}$$

where the functions $A$ and $B$ take simple forms in the $N_{\rm sat} \gg \bar{N}$ limit:

$$A(\gamma, \bar{N}) = \begin{cases} \frac{1-e^{-1/\bar{N}}}{N_{\rm sat}^2} \frac{\exp\left[(2/\gamma-1)N_{\rm sat}/\bar{N}\right]}{\exp\left[(2/\gamma-1)/\bar{N}\right]-1} & \text{if } \gamma < 2 \\ \left(1 - e^{-1/\bar{N}}\right) e^{(1-2/\gamma)/\bar{N}} \mathrm{Li}_2\left[e^{(2/\gamma-1)/\bar{N}}\right] & \text{if } \gamma > 2 \end{cases} \tag{S33a}$$

$$B(\gamma, \bar{N}) = \begin{cases} \frac{1-e^{-1/\bar{N}}}{N_{\rm sat}} \frac{\exp\left[(1/\gamma-1)N_{\rm sat}/\bar{N}\right]}{\exp\left[(1/\gamma-1)/\bar{N}\right]-1} & \text{if } \gamma < 1 \\ \left(1 - e^{-1/\bar{N}}\right) e^{(1-1/\gamma)/\bar{N}} \ln\left[\frac{1}{1-\exp\left[(1/\gamma-1)/\bar{N}\right]}\right] & \text{if } \gamma > 1 \end{cases}. \tag{S33b}$$

Here $\mathrm{Li}_2$ denotes the polylogarithm function of order 2, which is defined as $\mathrm{Li}_2(x) = \sum_{k=1}^{\infty} x^k/k^2$.

The three successive regimes described by Eqs. (S30-S32) are clearly apparent in Fig. S7.

[1] Christophe Texier. Individual energy level distributions for one-dimensional diagonal and off-diagonal disorder. *J. Phys. A Math. Gen.*, 33:6095–6128, 2000.

[2] N G Van Kampen. *Stochastic Processes in Physics and Chemistry*. North-Holland, Amsterdam, 1992.